Multibody System Dynamics
https://doi.org/10.1007/s11044-024-09986-0

RESEARCH

Beam modeling in a floating frame of reference for torsion dynamics of helicopter rotor blades

Felix Weiss[1] · **Joshua Merlis**[1]

Received: 5 December 2023 / Accepted: 9 April 2024

Abstract
In the ongoing development of DLR's Versatile Aeromechanics Simulation Tool, an elastic-beam model is integrated into the multibody system based on the floating frame-of-reference formulation. Although the application of this formulation for one-dimensional beam models has already been addressed in the literature, the challenge remains to properly model the torsion dynamics of rotor blades – especially under high centrifugal loads. To this aim, this work suggests the consideration of rotational shape functions in the inertia shape integrals and in the application of gravitational, inertial, and external loads. This modified approach is validated based on the structural analysis of a rotor blade with complex geometrical properties.

Keywords Torsion dynamics · Inertia shape integrals · Centrifugal loads · Rotational shape functions · Propeller moment

Nomenclature

Abbreviations

BAM	Beam Advanced Model
DLR	German Aerospace Center
FE	Finite Element
FFR	Floating Frame-of-Reference
Fi	ith blade flap mode, $i = 1, 2, 3, \ldots$
Li	ith blade lead-lag mode, $i = 1, 2, 3, \ldots$
MBS	Multibody System
ODE	Ordinary Differential Equations
Ti	ith blade torsion mode, $i = 1, 2, 3, \ldots$
VAST	Versatile Aeromechanics Simulation Tool

Symbols

A (m^2)	area

✉ F. Weiss
felix.weiss@dlr.de

[1] German Aerospace Center (DLR), Institute of Flight Systems, Lilienthalplatz 7, 38108 Braunschweig, Germany

Published online: 22 April 2024

$\mathbf{a}$ (m/s^2)	translatory acceleration of the FFR
a, c (m)	side lengths
$\mathbf{D}_{\mathrm{ff}}$ (Nms)	damping matrix of FE system
E (N/m^2)	Young's modulus
$\mathbf{F}$ (N)	force vector
$\mathbf{g}$ (m/s^2)	gravitational acceleration
I_{ij} (div.)	cross-sectional mass moment of order $ij = 00, 10, 01, 20, 02, 11$
$\bar{\mathbf{J}}_{\theta\mathrm{f}}$ (kgm^2)	coupling matrix: rigid rotational – flexible
$\bar{\mathbf{J}}_{\theta\theta}$ (kgm^2)	rigid rotational inertia tensor
$\mathbf{K}_{\mathrm{ff}}$ (Nm)	stiffness matrix of FE system
k (Nm/rad)	torsional stiffness
$\mathbf{M}$ (Nm)	moment vector
$\mathbf{M}_{\mathrm{ff}}$ (kgm^2)	mass matrix of FE system
m (kg)	mass
$\mathbf{m}_{\mathrm{RR}}$ (kg)	rigid translatory mass matrix
$\mathbf{Q}$ (div.)	right-hand side load terms
R (m)	radius
$\mathbf{r}_{\mathrm{I}}$ ($-$)	flexible position states
$\mathbf{r}_{\mathrm{II}}$ (1/s)	flexible velocity states, $\mathbf{r}_{\mathrm{II}} = \dot{\mathbf{r}}_{\mathrm{I}}$
$\mathbf{S}$ (m)	complemented shape function matrix $\mathbf{S} = \mathbf{S}_{\mathrm{tra}} - \tilde{\mathbf{u}}_{\mathrm{A}}\,\mathbf{S}_{\mathrm{rot}}$
$\mathbf{S}_{\mathrm{rot}}$ (rad)	rotational shape function matrix
$\mathbf{S}_{\mathrm{tra}}$ (m)	translatory shape function matrix
$\bar{\mathbf{S}}$ (kgm)	coupling matrix: rigid translatory – flexible
$\tilde{\bar{\mathbf{S}}}_{\mathrm{t}}$ (kgm)	coupling matrix: rigid translatory – rigid rotational
$\mathbf{T}$ ($-$)	rotation matrix: FFR to local cross-sectional frame
$\bar{\mathbf{u}}$ (m)	position vector relative to the FFR
$\mathbf{u}_{\mathrm{A}}$ (m)	position vector within the cross-section
$\bar{\mathbf{u}}_{\mathrm{m}}$ (m)	cross-sectional reference location relative to the FFR
u, v, w (m)	translatory flexible deflections in directions ζ, ξ, η
V (m^3)	volume
$\mathbf{v}$ (m/s)	translatory velocity vector
x, y, z (m)	coordinates in the FFR
ζ (m)	coordinate along the reference axis
η (m)	vertical coordinate orthogonal to the reference axis
ϑ (°)	inclination
ξ (m)	lateral coordinate orthogonal to the reference axis
ρ (kg/m^3)	mass density
Φ, Φ_ξ, Φ_η (rad)	rotational flexible deflections around ζ, ξ, η
Ω (rad/s)	rotor speed
ω (rad/s)	angular velocity vector

Indices, accentuations, and operators

$()_{\mathrm{c}}$	centrifugal
$()_{\mathrm{e}}$	external
$()^{\mathrm{f}}$	flexible motion
$()_{\mathrm{flex}}$	due to deformation
$()_{\mathrm{g}}$	gravitational
$()^{\mathrm{loc}}$	in local cross-sectional frame
$()_{\mathrm{p}}$	related to the propeller moment

$()_{\mathrm{pre}}$	undeformed (e.g., pretwist)
$()^{\mathrm{R}}$	rigid translatory motion
$()_{\mathrm{v}}$	inertial
$()^{\theta}$	rigid rotational motion
$\dot{\mathbf{X}}$	time derivative of $\mathbf{X}$
$\mathbf{X}'$	spatial derivative of $\mathbf{X}$
$\bar{\mathbf{X}}$	vector $\mathbf{X}$ is given relative to the FFR
$\mathbf{X}^{\mathrm{T}}$	transpose of $\mathbf{X}$
$\tilde{\mathbf{X}}$	cross product operator for vector $\mathbf{X}$

1 Introduction

Helicopter rotor blades are usually slender structures with a rotor radius much larger than the chord length and thickness. This geometrical property encourages modeling the blade as a one-dimensional (1D) beam, which saves computational costs compared to a 3D structural model. For this reason, multiphysics tools for helicopter (rotor) simulations – so-called comprehensive codes – commonly employ beam models to simulate the blades. This approach is also taken in the Versatile Aeromechanics Simulation Tool (VAST) [3].

VAST's structural kernel is a multibody system (MBS) that includes both rigid and flexible bodies. The MBS formalism is based on a set of minimal states that are comprised of the joint states and the states representing flexible-body deformation. This method yields ordinary differential equations (ODE) of motion, which is a requirement for each of the various VAST models (MBS, airloads, inflow, control, etc.) that are coupled to each other by the VAST solver.[1] The ODE formalism requires the Jacobians of the bodies' linear and angular velocities $\mathbf{v}$ and ω as well as the flexible velocities $\mathbf{r}_{\mathrm{II}}$ with respect to the minimal states of the whole MBS. These Jacobians are calculated using automatic differentiation [6]. This not only improves the maintainability of the code, but also substantially simplifies the inclusion of flexible body models.

The use cases of VAST include flexible structures (e.g., rotor blades, fuselage, tail boom) that undergo large reference displacements, but only small deformations. Under these conditions, the floating frame-of-reference (FFR) formulation [8, 9] is applicable with good accuracy. At the same time, this method allows various types of flexible-body models to be included, such as finite-element (FE) models or modal descriptions of deformation. For these reasons, the FFR formulation is used instead of other approaches, e.g., the absolute nodal coordinate formulation or the geometrically exact beam formulation (both compared in [1]), although these are superior to the FFR formulation if geometric nonlinearities play a role, i.e., in large deformation analyses.

For flexible bodies in VAST, the nodal position states $\mathbf{r}_{\mathrm{I}}$ and velocity states $\mathbf{r}_{\mathrm{II}}$ of the FE model describe the body deformation with respect to the FFR, which moves ("floats") relative to the inertial frame by $\mathbf{v}$ and ω. The vectors $\mathbf{v}$ and ω are expressed in the coordinates of the FFR.[2] These vectors represent the rigid-body portion of motion with the corresponding mass matrix $\mathbf{m}_{\mathrm{RR}}$, inertia tensor $\bar{\mathbf{J}}_{\theta\theta}$, and coupling matrix $\tilde{\bar{\mathbf{S}}}_{\mathrm{t}}^{\mathrm{T}}$, see the upper part of equa-

[1] In particular, differential algebraic equations (DAE) are not allowed for an individual VAST model.

[2] The time derivative of the FFR's position in the inertial frame reads $\dot{\mathbf{x}} = \mathbf{R}\,\mathbf{v}$, while the rotation $\mathbf{R}$ from the FFR to the inertial coordinate system is internally handled by a quaternion. The quaternion's time derivative is based on the rotated angular velocity $\mathbf{R}\,\omega$.

tion (1):

$$\begin{bmatrix} \mathbf{m}_{\mathrm{RR}} & \tilde{\bar{\mathbf{S}}}_{\mathrm{t}}^{\mathrm{T}} & \bar{\mathbf{S}} \\ & \bar{\mathbf{J}}_{\theta\theta} & \bar{\mathbf{J}}_{\theta\mathrm{f}} \\ sym. & & \mathbf{M}_{\mathrm{ff}} \end{bmatrix} \begin{bmatrix} \dot{\mathbf{v}} \\ \dot{\omega} \\ \dot{\mathbf{r}}_{\mathrm{II}} \end{bmatrix} = \begin{bmatrix} \mathbf{0} \\ \mathbf{0} \\ -\mathbf{K}_{\mathrm{ff}}\,\mathbf{r}_{\mathrm{I}} - \mathbf{D}_{\mathrm{ff}}\,\mathbf{r}_{\mathrm{II}} \end{bmatrix} + \begin{bmatrix} \mathbf{Q}_{\mathrm{g}}^{\mathrm{R}} \\ \mathbf{Q}_{\mathrm{g}}^{\theta} \\ \mathbf{Q}_{\mathrm{g}}^{\mathrm{f}} \end{bmatrix} + \begin{bmatrix} \mathbf{Q}_{\mathrm{v}}^{\mathrm{R}} \\ \mathbf{Q}_{\mathrm{v}}^{\theta} \\ \mathbf{Q}_{\mathrm{v}}^{\mathrm{f}} \end{bmatrix} + \begin{bmatrix} \mathbf{Q}_{\mathrm{e}}^{\mathrm{R}} \\ \mathbf{Q}_{\mathrm{e}}^{\theta} \\ \mathbf{Q}_{\mathrm{e}}^{\mathrm{f}} \end{bmatrix}. \quad (1)$$

The second-order differential equation of the FE system has been converted to a first-order form; the trivial kinematic equation $\dot{\mathbf{r}}_{\mathrm{I}} = \mathbf{r}_{\mathrm{II}}$ is solved separately. In the lower part of equation (1), the FE system's mass $\mathbf{M}_{\mathrm{ff}}$, stiffness $\mathbf{K}_{\mathrm{ff}}$, and damping $\mathbf{D}_{\mathrm{ff}}$ matrices are found. $\mathbf{K}_{\mathrm{ff}}$ is composed of both the structural and geometric stiffnesses. $\mathbf{D}_{\mathrm{ff}}$ depends on the structural damping model. In this paper, no structural damping is applied, i.e., $\mathbf{D}_{\mathrm{ff}} = \mathbf{0}$. The rightmost entries $\bar{\mathbf{S}}$ and $\bar{\mathbf{J}}_{\theta\mathrm{f}}$ in the upper part of the overall mass matrix constitute coupling terms between the rigid-body motion and the flexible motion. The right-hand side includes gravitational loads $\mathbf{Q}_{\mathrm{g}}$, inertial loads $\mathbf{Q}_{\mathrm{v}}$, and external loads $\mathbf{Q}_{\mathrm{e}}$ acting on the rigid translatory, rigid rotational, and flexible motion (superscripts R, θ, and f, respectively). In the MBS, equation (1) is evaluated for the whole FE system, i.e., for the assembly of all finite elements. Accordingly, in equation (1), $\mathbf{r}_{\mathrm{I}}$ and $\mathbf{r}_{\mathrm{II}}$ represent the states of all nodes. For the remainder of the paper, in contrast, $\mathbf{r}_{\mathrm{I}}$ and $\mathbf{r}_{\mathrm{II}}$ represent the states of one element only (featuring 2 nodes). All matrices and vectors given below refer to this one element.

The set of nodal states $(\mathbf{r}_{\mathrm{I}}, \mathbf{r}_{\mathrm{II}})$, the assembly of $\mathbf{K}_{\mathrm{ff}}$, as well as a predominant portion of the shape functions that are referenced in the following are based on the Beam Advanced Model (BAM)[3] [10–12]. BAM is specialized to address the needs of helicopter-blade modeling. Through the introduction of differential degrees-of-freedom,[4] it enables the efficient computation of discontinuous physical characteristics, without the need for a refined discretization. BAM accounts for geometric stiffening by integrating the stress distribution in the deformed configuration over the element, as described in [12, equation 22] and [11, equations 30 and 34]. This means that $\mathbf{K}_{\mathrm{ff}} = \mathbf{K}_{\mathrm{ff}}(\mathbf{r}_{\mathrm{I}})$. Prior to the work at hand, BAM had been integrated into the comprehensive code HOST in a prototypical fashion based on decoupled dynamic equations for the rigid- and flexible-body motions [13]. In contrast, to address the couplings between these kinds of motion as well as interactions with other bodies, BAM is integrated into the MBS of VAST via the FFR approach.

In [12, equations 32 – 35], shape functions based on third-order Hermite polynomials are defined for the translatory deflections $u(\zeta)$, $v(\zeta)$, $w(\zeta)$, and the torsional deflection $\Phi(\zeta)$ of a BAM element. ζ is the coordinate along the reference axis. That work also derives expressions [12, equations 8 and 9] for the bending angles $\Phi_\xi(\zeta)$, $\Phi_\eta(\zeta)$ about the lateral axis ξ and the vertical axis η, respectively, using Timoshenko beam theory to link these to the translatory bending. Based on these relationships, the element's translatory and rotational shape function matrices $\mathbf{S}_{\mathrm{tra}}$ and $\mathbf{S}_{\mathrm{rot}}$ are defined as

$$\begin{bmatrix} u(\zeta) \\ v(\zeta) \\ w(\zeta) \end{bmatrix} = \mathbf{S}_{\mathrm{tra}}(\zeta)\,\mathbf{r}_{\mathrm{I}} \quad \text{and} \quad \begin{bmatrix} \Phi(\zeta) \\ \Phi_\xi(\zeta) \\ \Phi_\eta(\zeta) \end{bmatrix} = \mathbf{S}_{\mathrm{rot}}(\zeta)\,\mathbf{r}_{\mathrm{I}}, \quad (2)$$

with $\mathbf{r}_{\mathrm{I}}$ representing the degrees-of-freedom of the BAM element. The indices 1 and 2 denote the respective node of the element, while l and r indicate the left and right side of the node,

[3] Since the underlying Ph.D. thesis of BAM [10] is still under embargo at the time of publication of the paper at hand, the publicly available references [11, 12] are provided additionally.

[4] Included are the derivatives with respect to the beam's length axis of the axial elongation (u') and torsion about this axis (Φ'), at locations immediately to each side of the node.

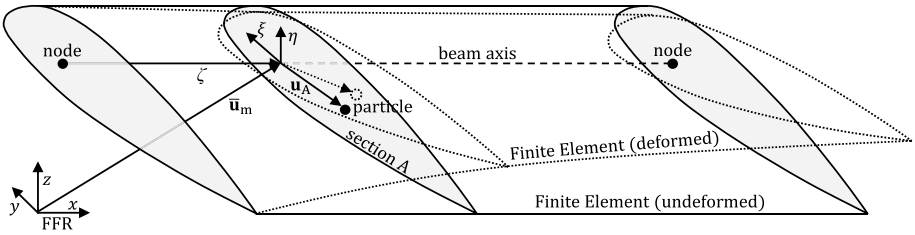

Fig. 1 Particle in a cross-section A moving due to torsional deformation of a 1D beam

respectively:

$$\mathbf{r}_{\mathrm{I}} = \big(u_1, v_1, w_1, \Phi_1, \Phi_{\xi,1}, \Phi_{\eta,1}, u'_{1,l}, u'_{1,r}, \Phi'_{1,l}, \Phi'_{1,r}, u_2, v_2, w_2, \Phi_2, \Phi_{\xi,2}, \Phi_{\eta,2}, u'_{2,l}, u'_{2,r}, \Phi'_{2,l}, \Phi'_{2,r}\big)^{\mathrm{T}}. \tag{3}$$

Translatory shape function matrices are also applied in the FFR formulation [7, 9], where deformations read $\mathbf{S}_{\mathrm{tra}}\,\mathbf{r}_{\mathrm{I}}$ and deformation velocities read $\mathbf{S}_{\mathrm{tra}}\,\mathbf{r}_{\mathrm{II}}$. The sole use of $\mathbf{S}_{\mathrm{tra}}$ for these kinematic evaluations works fine as long as $\mathbf{S}_{\mathrm{tra}}$ resolves all spatial dimensions, i.e., $\mathbf{S}_{\mathrm{tra}} = \mathbf{S}_{\mathrm{tra}}(x, y, z)$, with x, y, z being the coordinates with respect to the FFR. However, this is not the case for a 1D beam model, where $\mathbf{S}_{\mathrm{tra}} = \mathbf{S}_{\mathrm{tra}}(\zeta)$ depends only on the beam-axis coordinate ζ. For such beam models, the consideration of the *rotational* shape function matrix $\mathbf{S}_{\mathrm{rot}}$ may be necessary to evaluate the *translatory* kinematics of a particle in the body, as shown in the following.

Figure 1 illustrates a deformed finite beam element. The reference point of the cross-section A is located at $\bar{\mathbf{u}}_{\mathrm{m}}$. The bar indicates that the quantity is given relative to the FFR. The particle under consideration is located at a distance $\mathbf{u}_{\mathrm{A}}$ from the reference axis, so that the particle's location with respect to the FFR reads

$$\bar{\mathbf{u}} = \bar{\mathbf{u}}_{\mathrm{m}} + \mathbf{u}_{\mathrm{A}}. \tag{4}$$

Its velocity is

$$\dot{\bar{\mathbf{u}}} = \dot{\bar{\mathbf{u}}}_{\mathrm{m}} + \dot{\mathbf{u}}_{\mathrm{A}} = \mathbf{S}_{\mathrm{tra}}(\zeta)\,\mathbf{r}_{\mathrm{II}} + \tilde{\omega}_{\mathrm{flex}}\mathbf{u}_{\mathrm{A}}, \tag{5}$$

with $\omega_{\mathrm{flex}} = \mathbf{S}_{\mathrm{rot}}(\zeta)\,\mathbf{r}_{\mathrm{II}}$ and the tilde symbol denoting the cross product operator according to

$$\mathbf{a} \times \mathbf{b} = \begin{bmatrix} a_2 b_3 - a_3 b_2 \\ a_3 b_1 - a_1 b_3 \\ a_1 b_2 - a_2 b_1 \end{bmatrix} = \tilde{\mathbf{a}}\mathbf{b} = \begin{bmatrix} 0 & -a_3 & a_2 \\ a_3 & 0 & -a_1 \\ -a_2 & a_1 & 0 \end{bmatrix} \begin{bmatrix} b_1 \\ b_2 \\ b_3 \end{bmatrix}. \tag{6}$$

Equation (5) becomes

$$\dot{\bar{\mathbf{u}}} = \mathbf{S}_{\mathrm{tra}}(\zeta)\,\mathbf{r}_{\mathrm{II}} - \tilde{\mathbf{u}}_{\mathrm{A}}\,\mathbf{S}_{\mathrm{rot}}(\zeta)\,\mathbf{r}_{\mathrm{II}} = \underbrace{\left[\mathbf{S}_{\mathrm{tra}}(\zeta) - \tilde{\mathbf{u}}_{\mathrm{A}}\,\mathbf{S}_{\mathrm{rot}}(\zeta)\right]}_{\mathbf{S}}\,\mathbf{r}_{\mathrm{II}}, \tag{7}$$

where the change from + to − is explained by $\tilde{\mathbf{a}}\mathbf{b} = -\tilde{\mathbf{b}}\mathbf{a}$. The term

$$\mathbf{S}(\zeta, \xi, \eta) = \mathbf{S}_{\text{tra}}(\zeta) - \tilde{\mathbf{u}}_{\text{A}}(\xi, \eta)\, \mathbf{S}_{\text{rot}}(\zeta) \tag{8}$$

is called the complemented shape function matrix in this work. Due to $\mathbf{u}_{\text{A}} = \mathbf{u}_{\text{A}}(\xi, \eta)$, it depends not only on ζ, but also on the cross-sectional coordinates ξ and η.

In addition to its kinematic impact, $\mathbf{S}_{\text{rot}}$ is also important for the dynamics of the flexible-beam model. According to the FFR theory [7, 9], several submatrices and vectors of equation (1) include volume integrals with both the mass density $\rho(x, y, z)$ and the translatory shape function matrix $\mathbf{S}_{\text{tra}}(x, y, z)$ as integrands – the so-called inertia shape integrals. As in the kinematic example above, however, the sole consideration of $\mathbf{S}_{\text{tra}}$ may be insufficient for capturing dynamic effects related to torsional deformation. The first results of additionally considering $\mathbf{S}_{\text{rot}}$ in the inertial loads $\mathbf{Q}_{\text{v}}^{\text{f}}$ were presented in [14]. In the present work, the complemented shape function matrix $\mathbf{S}$ is consistently used instead of $\mathbf{S}_{\text{tra}}$ in all inertia shape integrals and all right-hand side load terms of equation (1). In Sect. 2, the individual terms are given based on $\mathbf{S}$ according to equation (8). The benefit of the modified implementation ($\mathbf{S}$ instead of $\mathbf{S}_{\text{tra}}$) in the analysis of rotating beams, especially helicopter rotor blades, is presented in Sect. 3.

2 Theory

The terms of equation (1) are taken from the literature [7, 9] in their general 3D formulation. This section presents two modifications of the terms:

- The 3D volume integrals are transformed to 1D integrals along the beam's length. The preevaluated cross-sectional integrals, which are included in the beam model's configuration data, appear as integrands. This transformation improves performance and facilitates the configuration of beam models.
- The complemented shape function matrix $\mathbf{S} = \mathbf{S}_{\text{tra}} - \tilde{\mathbf{u}}_{\text{A}}\, \mathbf{S}_{\text{rot}}$ is consistently applied.

2.1 Cross-sectional mass moments in the local frame

First, the following cross-sectional integrals are defined. In the local cross-sectional frame, the offset $\mathbf{u}_{\text{A}}^{\text{loc}}$ of a particle from the cross-sectional reference (beam-axis intersection point) reads $\mathbf{u}_{\text{A}}^{\text{loc}} = (0, \xi, \eta)^{\text{T}}$. Table 1 lists the cross-sectional mass moments in the local frame. These are included in the beam model's configuration data and do not depend on deformation, so they can be evaluated in advance.

Table 1 Cross-sectional mass moments, integrated in the local cross-sectional frame

0th order	$I_{00} = \int_A \rho \, \mathrm{d}A$		
1st order	$I_{10} = \int_A \rho \, \xi \, \mathrm{d}A$	$I_{01} = \int_A \rho \, \eta \, \mathrm{d}A$	
2nd order	$I_{20} = \int_A \rho \, \xi^2 \, \mathrm{d}A$	$I_{02} = \int_A \rho \, \eta^2 \, \mathrm{d}A$	$I_{11} = \int_A \rho \, \xi \, \eta \, \mathrm{d}A$

2.2 Cross-sectional mass moments in the FFR

The transformation matrix $\mathbf{T}$ rotates vectors and matrices from the FFR to the local cross-sectional frame. Thus, the application of $\mathbf{T}^{\mathrm{T}}\mathbf{v}$ for vectors $\mathbf{v}$ and $\mathbf{T}^{\mathrm{T}}\mathbf{M}\mathbf{T}$ for matrices $\mathbf{M}$ rotates from the local frame to the FFR. The FFR-transformed vectors and matrices are:

$$\int_A \rho \, \mathrm{d}A = I_{00} \tag{9}$$

$$\int_A \rho \mathbf{u}_{\mathrm{A}} \, \mathrm{d}A = \mathbf{T}^{\mathrm{T}} \begin{bmatrix} 0 \\ I_{10} \\ I_{01} \end{bmatrix} \quad \text{or} \quad \int_A \rho \tilde{\mathbf{u}}_{\mathrm{A}} \, \mathrm{d}A = \mathbf{T}^{\mathrm{T}} \begin{bmatrix} 0 & -I_{01} & I_{10} \\ I_{01} & 0 & 0 \\ -I_{10} & 0 & 0 \end{bmatrix} \mathbf{T} \tag{10}$$

$$\int_A \rho \tilde{\mathbf{u}}_{\mathrm{A}}^{\mathrm{T}} \tilde{\mathbf{u}}_{\mathrm{A}} \, \mathrm{d}A = \mathbf{T}^{\mathrm{T}} \begin{bmatrix} I_{20} + I_{02} & 0 & 0 \\ 0 & I_{02} & -I_{11} \\ 0 & -I_{11} & I_{20} \end{bmatrix} \mathbf{T} \tag{11}$$

$$\int_A \rho \mathbf{u}_{\mathrm{A}} \mathbf{u}_{\mathrm{A}}^{\mathrm{T}} \, \mathrm{d}A = \mathbf{T}^{\mathrm{T}} \begin{bmatrix} 0 & 0 & 0 \\ 0 & I_{20} & I_{11} \\ 0 & I_{11} & I_{02} \end{bmatrix} \mathbf{T}. \tag{12}$$

$\mathbf{T}$ includes two rotations:

1. The orientation of the local frame with respect to the FFR in the undeformed configuration. This contribution can be large, e.g., when the beam axis is bent, as is the case for some modern helicopter rotor blades like the one investigated in Sect. 3.3.
2. The flexible rotation due to deformation of the beam. This part is usually small but can be important – especially for the torsional dynamics, as presented in Sect. 3.2.

Consequently, the deformation states $\mathbf{r}_{\mathrm{I}}$ affect the rotation matrix $\mathbf{T}$ in equations (10)–(12), so that these integrals – when expressed in the FFR – depend on the deformation of the beam as well.

2.3 Inertia shape integrals

The particle's location relative to the FFR is given by equation (4), where $\bar{\mathbf{u}}_{\mathrm{m}}$ is the cross-sectional reference location (affected by translatory flexible displacements), and $\mathbf{u}_{\mathrm{A}}$ is the offset within the cross-section (affected by rotational flexible displacements). This composition is used in the following for the transformation of the 3D integrals over the volume V to 1D integrals along the beam axis ζ. The integrals over the cross-sectional area A (equations (9)–(12)) are highlighted in gray color to make them more easily recognizable. The integrals corresponding to rigid-body motion (not affected by the introduction of the complemented shape function matrix) are:

$$\mathbf{m}_{\mathrm{RR}} = \int_V \rho \, \mathbf{I} \, \mathrm{d}V = \mathbf{I} \int_\zeta \int_A \rho \mathrm{d}A \, \mathrm{d}\zeta \tag{13}$$

$$\bar{\mathbf{S}}_{\mathrm{t}} = \int_V \rho \, \bar{\mathbf{u}} \, \mathrm{d}V = \int_\zeta \int_A \rho \, (\bar{\mathbf{u}}_{\mathrm{m}} + \mathbf{u}_{\mathrm{A}}) \, \mathrm{d}A \, \mathrm{d}\zeta = \int_\zeta \left[\bar{\mathbf{u}}_{\mathrm{m}} \int_A \rho \, \mathrm{d}A + \int_A \rho \, \mathbf{u}_{\mathrm{A}} \, \mathrm{d}A \right] \mathrm{d}\zeta \tag{14}$$

$$\bar{\mathbf{J}}_{\theta\theta} = \int_V \rho \, \tilde{\bar{\mathbf{u}}}^{\mathrm{T}} \tilde{\bar{\mathbf{u}}} \, \mathrm{d}V = \int_\zeta \int_A \rho (\widetilde{\bar{\mathbf{u}}_{\mathrm{m}} + \mathbf{u}_{\mathrm{A}}})^{\mathrm{T}} (\widetilde{\bar{\mathbf{u}}_{\mathrm{m}} + \mathbf{u}_{\mathrm{A}}}) \, \mathrm{d}A \, \mathrm{d}\zeta$$

$$= \int_\zeta \left[\tilde{\bar{\mathbf{u}}}_\mathrm{m}^\mathrm{T} \tilde{\bar{\mathbf{u}}}_\mathrm{m} \int_A \rho \, \mathrm{d}A + \tilde{\bar{\mathbf{u}}}_\mathrm{m}^\mathrm{T} \int_A \rho \tilde{\mathbf{u}}_\mathrm{A} \, \mathrm{d}A + \int_A \rho \tilde{\mathbf{u}}_\mathrm{A}^\mathrm{T} \, \mathrm{d}A \, \tilde{\bar{\mathbf{u}}}_\mathrm{m} + \int_A \rho \tilde{\mathbf{u}}_\mathrm{A}^\mathrm{T} \tilde{\mathbf{u}}_\mathrm{A} \, \mathrm{d}A \right] \mathrm{d}\zeta. \quad (15)$$

The integrals related to flexible motion are based on the complemented shape function matrix $\mathbf{S}$ according to equation (8). These are:

$$\begin{aligned}
\bar{\mathbf{S}} &= \int_V \rho \, \mathbf{S} \, \mathrm{d}V = \int_\zeta \int_A \rho \left(\mathbf{S}_\mathrm{tra} - \tilde{\mathbf{u}}_\mathrm{A} \mathbf{S}_\mathrm{rot} \right) \mathrm{d}A \, \mathrm{d}\zeta \\
&= \int_\zeta \left[\mathbf{S}_\mathrm{tra} \int_A \rho \, \mathrm{d}A - \int_A \rho \tilde{\mathbf{u}}_\mathrm{A} \, \mathrm{d}A \, \mathbf{S}_\mathrm{rot} \right] \mathrm{d}\zeta \qquad (16) \\
\bar{\mathbf{J}}_{\theta\mathrm{f}} &= \int_V \rho \, \tilde{\bar{\mathbf{u}}} \, \mathbf{S} \, \mathrm{d}V = \int_\zeta \int_A \rho \left(\widetilde{\bar{\mathbf{u}}_\mathrm{m} + \mathbf{u}_\mathrm{A}} \right) \left(\mathbf{S}_\mathrm{tra} - \tilde{\mathbf{u}}_\mathrm{A} \mathbf{S}_\mathrm{rot} \right) \mathrm{d}A \, \mathrm{d}\zeta \\
&= \int_\zeta \left[\left(\tilde{\bar{\mathbf{u}}}_\mathrm{m} \int_A \rho \, \mathrm{d}A + \int_A \rho \tilde{\mathbf{u}}_\mathrm{A} \, \mathrm{d}A \right) \mathbf{S}_\mathrm{tra} \right. \\
&\quad \left. - \left(\tilde{\bar{\mathbf{u}}}_\mathrm{m} \int_A \rho \tilde{\mathbf{u}}_\mathrm{A} \, \mathrm{d}A - \int_A \rho \tilde{\mathbf{u}}_\mathrm{A}^\mathrm{T} \tilde{\mathbf{u}}_\mathrm{A} \, \mathrm{d}A \right) \mathbf{S}_\mathrm{rot} \right] \mathrm{d}\zeta \qquad (17) \\
\mathbf{M}_\mathrm{ff} &= \int_V \rho \, \mathbf{S}^\mathrm{T} \mathbf{S} \, \mathrm{d}V = \int_\zeta \int_A \rho \left(\mathbf{S}_\mathrm{tra} - \tilde{\mathbf{u}}_\mathrm{A} \mathbf{S}_\mathrm{rot} \right)^\mathrm{T} \left(\mathbf{S}_\mathrm{tra} - \tilde{\mathbf{u}}_\mathrm{A} \mathbf{S}_\mathrm{rot} \right) \mathrm{d}A \, \mathrm{d}\zeta \\
&= \int_\zeta \left[\mathbf{S}_\mathrm{tra}^\mathrm{T} \mathbf{S}_\mathrm{tra} \int_A \rho \, \mathrm{d}A - \mathbf{S}_\mathrm{tra}^\mathrm{T} \int_A \rho \tilde{\mathbf{u}}_\mathrm{A} \, \mathrm{d}A \, \mathbf{S}_\mathrm{rot} \right. \\
&\quad \left. - \mathbf{S}_\mathrm{rot}^\mathrm{T} \left(\int_A \rho \tilde{\mathbf{u}}_\mathrm{A} \, \mathrm{d}A \right)^\mathrm{T} \mathbf{S}_\mathrm{tra} + \mathbf{S}_\mathrm{rot}^\mathrm{T} \int_A \rho \tilde{\mathbf{u}}_\mathrm{A}^\mathrm{T} \tilde{\mathbf{u}}_\mathrm{A} \, \mathrm{d}A \, \mathbf{S}_\mathrm{rot} \right] \mathrm{d}\zeta. \qquad (18)
\end{aligned}$$

Note that $\mathbf{S}_\mathrm{tra} = \mathbf{S}_\mathrm{tra}(\zeta)$ and $\mathbf{S}_\mathrm{rot} = \mathbf{S}_\mathrm{rot}(\zeta)$. Along with the cross-sectional integrals' dependency on the deformation state $\mathbf{r}_\mathrm{I}$ due to flexible rotation (cf. Sect. 2.2), the integrals in equations (14), (15), and (17) also depend on the deformation because $\bar{\mathbf{u}}_\mathrm{m} = \bar{\mathbf{u}}_\mathrm{m}(\zeta, \mathbf{r}_\mathrm{I})$.

2.4 Load terms

Finally, the loads $\mathbf{Q}_\mathrm{g}^\mathrm{f}$, $\mathbf{Q}_\mathrm{v}^\mathrm{f}$, and $\mathbf{Q}_\mathrm{e}^\mathrm{f}$ also contain the shape function matrix $\mathbf{S}$. $\mathbf{g}$ denotes the gravitational acceleration expressed in the FFR, while $\mathbf{a}$ is the FFR acceleration due to angular velocities in the MBS:

$$\begin{aligned}
\mathbf{Q}_\mathrm{g}^\mathrm{f} &= \int_V \rho \, \mathbf{S}^\mathrm{T} \mathbf{g} \, \mathrm{d}V = \bar{\mathbf{S}}^\mathrm{T} \mathbf{g} \qquad (19) \\
\mathbf{Q}_\mathrm{v}^\mathrm{f} &= - \int_V \rho \, \mathbf{S}^\mathrm{T} \left(\mathbf{a} + \tilde{\omega}\tilde{\omega}\bar{\mathbf{u}} + 2\tilde{\omega}\dot{\bar{\mathbf{u}}} \right) \mathrm{d}V \\
&= - \int_\zeta \int_A \rho \left(\mathbf{S}_\mathrm{tra} - \tilde{\mathbf{u}}_\mathrm{A} \mathbf{S}_\mathrm{rot} \right)^\mathrm{T} \\
&\quad \cdot \left(\mathbf{a} + \tilde{\omega}\tilde{\omega} \left(\bar{\mathbf{u}}_\mathrm{m} + \mathbf{u}_\mathrm{A} \right) + 2\tilde{\omega} \left(\mathbf{S}_\mathrm{tra} - \tilde{\mathbf{u}}_\mathrm{A} \mathbf{S}_\mathrm{rot} \right) \mathbf{r}_\mathrm{II} \right) \mathrm{d}A \, \mathrm{d}\zeta \\
&= \int_\zeta \left[\mathbf{S}_\mathrm{tra}^\mathrm{T} \left((-\mathbf{a} - \tilde{\omega}\tilde{\omega}\bar{\mathbf{u}}_\mathrm{m} - 2\tilde{\omega} \, \mathbf{S}_\mathrm{tra} \, \mathbf{r}_\mathrm{II}) \int_A \rho \mathrm{d}A \right. \right.
\end{aligned}$$

$$
\begin{aligned}
&-\tilde{\omega}\tilde{\omega}\int_A \rho\mathbf{u}_\mathrm{A}\mathrm{d}A + 2\tilde{\omega}\int_A \rho\tilde{\mathbf{u}}_\mathrm{A}\mathrm{d}A\,\mathbf{S}_\mathrm{rot}\,\mathbf{r}_\mathrm{II}\Big) \\
&+\mathbf{S}_\mathrm{rot}^\mathrm{T}\left(\int_A \rho\tilde{\mathbf{u}}_\mathrm{A}^\mathrm{T}\mathrm{d}A\,(\mathbf{a}+\tilde{\omega}\tilde{\omega}\bar{\mathbf{u}}_\mathrm{m}+2\tilde{\omega}\,\mathbf{S}_\mathrm{tra}\,\mathbf{r}_\mathrm{II}) - \tilde{\omega}\int_A \rho\tilde{\mathbf{u}}_\mathrm{A}^\mathrm{T}\,\tilde{\mathbf{u}}_\mathrm{A}\,\mathrm{d}A\,\omega\right. \\
&\left.+2\left(\tilde{\omega}\int_A \rho\mathbf{u}_\mathrm{A}\,\mathbf{u}_\mathrm{A}^\mathrm{T}\,\mathrm{d}A - \int_A \rho\tilde{\mathbf{u}}_\mathrm{A}^\mathrm{T}\,\tilde{\mathbf{u}}_\mathrm{A}\,\mathrm{d}A\tilde{\omega}\right)\mathbf{S}_\mathrm{rot}\,\mathbf{r}_\mathrm{II}\right)\Big]\mathrm{d}\zeta
\end{aligned}
\tag{20}
$$

$$
\mathbf{Q}_\mathrm{e}^\mathrm{f} = \sum_{i=1}^{n}\mathbf{S}_\mathrm{tra}^\mathrm{T}(\zeta_i)\,\mathbf{F}_i + \mathbf{S}_\mathrm{rot}^\mathrm{T}(\zeta_i)\,\mathbf{M}_i\,. \tag{21}
$$

In equation (20), the conversions $\tilde{\mathbf{u}}_\mathrm{A}^\mathrm{T}\tilde{\omega}\tilde{\omega}\mathbf{u}_\mathrm{A} = -\tilde{\omega}\tilde{\mathbf{u}}_\mathrm{A}^\mathrm{T}\tilde{\mathbf{u}}_\mathrm{A}\omega$ and $-\tilde{\mathbf{u}}_\mathrm{A}^\mathrm{T}\tilde{\omega}\tilde{\mathbf{u}}_\mathrm{A} = \tilde{\omega}\mathbf{u}_\mathrm{A}\mathbf{u}_\mathrm{A}^\mathrm{T} - \tilde{\mathbf{u}}_\mathrm{A}^\mathrm{T}\tilde{\mathbf{u}}_\mathrm{A}\tilde{\omega}$ have been used. Equation (21) differs from the other load terms because the external loads $\mathbf{Q}_\mathrm{e}^\mathrm{f}$ are n pairs of discrete forces and moments $(\mathbf{F}_i, \mathbf{M}_i)$, while $\mathbf{Q}_\mathrm{g}^\mathrm{f}$ and $\mathbf{Q}_\mathrm{v}^\mathrm{f}$ are volume forces.

3 Results

The modified implementation has a significant influence on the inertial loads term $\mathbf{Q}_\mathrm{v}^\mathrm{f}$ acting on the flexible motion. The added value of using the complemented shape function matrix $\mathbf{S} = \mathbf{S}_\mathrm{tra} - \tilde{\mathbf{u}}_\mathrm{A}\,\mathbf{S}_\mathrm{rot}$ instead of the original shape function matrix $\mathbf{S} = \mathbf{S}_\mathrm{tra}$ for calculating $\mathbf{Q}_\mathrm{v}^\mathrm{f}$ is illustrated in the following. Section 3.2 verifies the implementation based on an academic test case with analytic reference results, and Sect. 3.3 presents results for a practical test case. Prior to these problem-specific results, a general verification based on a simple rotor blade is provided in Sect. 3.1.

3.1 General verification

The beam formulation presented in this paper is used for the modal analysis of a model helicopter rotor blade [15]. The rotor radius is 1.397 m, and the rotor speed varies between 0 and 660 rpm. The blade is attached to the hub at a radial station of 0.076 m (5.4% of the rotor radius) via hinges for flap (out-of-plane) and lead-lag (inplane) motion of the blade. The reference includes all the required configuration data of the structural model. It should be noted that the Young's modulus in [15] is given as $E = 1.0 \cdot 10^7\,\mathrm{lb/in^2}$, but its unit is obviously intended as $\mathrm{lbf/in^2}$.

The VAST beam model consists of 18 BAM elements. The corresponding radial stations of the nodes are listed in Table 2. 15 elements are required to account for the abrupt parameter changes along the radius according to [15, Table 1]. Three additional elements[5] are inserted in the uniform-blade section between $R = 0.718$ m and $R = 1.295$ m (51% to 93% of the radius).

In Fig. 2, the resulting eigenfrequencies ("VAST-BAM, $\mathbf{S} = \mathbf{S}_\mathrm{tra} - \tilde{\mathbf{u}}_\mathrm{A}\,\mathbf{S}_\mathrm{rot}$") are compared to the measured and predicted eigenfrequencies from [15], "TM4760". The two eigenfrequencies corresponding to the rigid-body flap and lead-lag modes (lowest two graphs) are not provided in [15]. The correlation between VAST-BAM and NASTRAN is very good. A discussion of the correlation between the numerical predictions and the experimental

[5] Only one element for the uniform section caused too high eigenfrequencies. The first seven eigenfrequencies converged with three or more additional elements for the uniform section.

Table 2 Nodal stations of the 18 BAM elements

R (m)	Comment	R (m)	Comment
0.076	hinge & FFR location	0.718	begin of uniform section
0.174		0.862	inserted
0.225		1.006	inserted
0.270		1.151	inserted
0.318		1.295	end of uniform section
0.330		1.340	
0.391		1.346	
0.453		1.372	
0.603		1.378	
...table continues to the right...		1.397	tip location

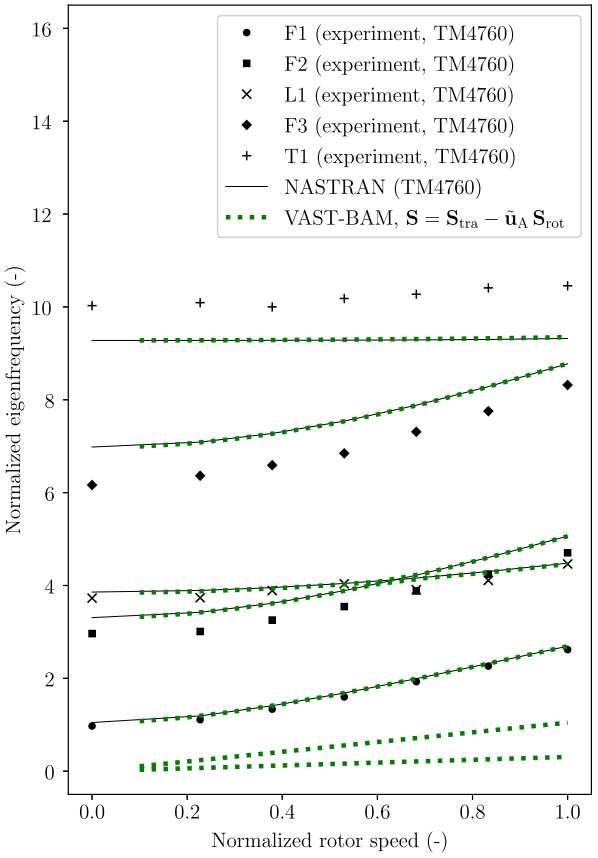

Fig. 2 Campbell diagram of the model helicopter rotor blade, all frequencies normalized to a nominal rotor speed of $\Omega = 69.115\,\text{rad/s}$ (660 rpm), configuration data and reference results (TM4760) taken from [15]

eigenfrequencies is omitted because it is unclear how the beam configuration data in [15, Table 1] has been determined. Accordingly, this test case constitutes a code-to-code verification only.

3.2 Verification of torsion dynamics based on an academic test case

The modified implementation including $\mathbf{S}_{\text{rot}}$ accounts for the effect of inertial loads on the beam's nodes' flexible rotation. One particularly relevant effect of inertial loads on flexible rotation in helicopter rotor analysis is the propeller moment [2, 5], which is illustrated in Fig. 3. The cross-section of a 1D beam may have different inertial properties in its two directions. For example, the lead-lag inertia per unit length of a typical rotor blade cross-section is larger than its flap inertia per unit length. In this case, for a rotating blade, the centrifugal forces $\mathbf{F}_{\text{c}}$ generate the propeller moment $\mathbf{M}_{\text{p}}$ that tends to rotate the section such that it lays flat in the plane of rotation.

The configuration used to verify the propeller moment is sketched in Fig. 4. The "beam" consists of four quasimassless[6] and torsionally compliant FE elements (thin part of the beam), which together have the torsional stiffness k. The fifth and last element is a quasi-rigid[7] cuboid of size $a \cdot a \cdot c$ with homogeneous mass density ρ (thick tip of the beam). Note that the beam axis ζ is not bent, i.e., the cuboid's longitudinal axis coincides with one of its shorter dimensions a and not with the longer side c. The beam is clamped to a hub with a constant rotational speed Ω and has an undeformed inclination of ϑ_{pre}. Due to the propeller moment acting on the cuboid, the beam is elastically twisted by $\vartheta_{\text{flex}} < 0$.

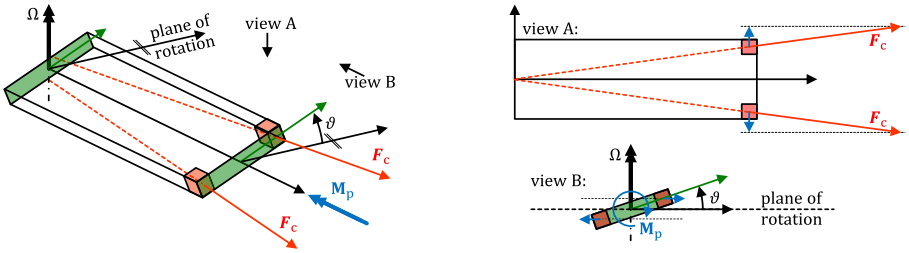

Fig. 3 Phenomenological explanation of the propeller moment $\mathbf{M}_{\text{p}}$

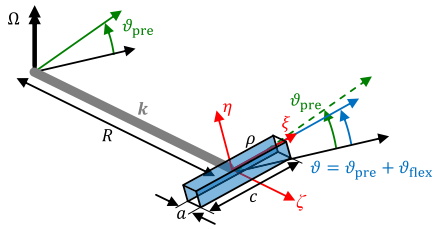

$$\Omega = 100\,\text{rad/s}$$
$$\vartheta_{\text{pre}} = 1\,^\circ$$
$$k = 2777.5\,\text{Nm/rad}$$
$$R = 10\,\text{m}$$
$$a = 0.01\,\text{m}$$
$$c = 1.0\,\text{m}$$
$$\rho = 1 \cdot 10^5\,\text{kg/m}^3$$

Fig. 4 Beam configuration for verifying the propeller moment

[6] The mass per length of the quasimassless beam elements is $m' = 1 \cdot 10^{-6}\,\text{kg/m}$.

[7] The Young's modulus of the quasirigid beam element is $E = 1 \cdot 10^{12}\,\text{N/m}^2$.

The propeller moment on the cuboid with inclination $\vartheta = \vartheta_{\text{pre}} + \vartheta_{\text{flex}}$ is

$$M_{\text{p}} = -\Omega^2 \cdot \left(I_{\eta\eta} - I_{\xi\xi}\right) \cdot \sin(\vartheta) \cdot \cos(\vartheta), \tag{22}$$

where the mass moments of inertia are $I_{\eta\eta} = m/12\,\left(a^2 + c^2\right)$ around the vertical axis and $I_{\xi\xi} = m/12\,\left(a^2 + a^2\right)$ around the transverse axis, both with $m = \rho\, a^2\, c$. The expression given in equation (22) can, for example, be identified in the torsional differential equation presented in [4] and is explicitly called "propeller moment" in [2]. The torsional stiffness of the rotating beam in equilibrium counteracts the propeller moment, i.e., $\vartheta_{\text{flex}} = M_{\text{p}}/k$. Since $\vartheta < 1\,^\circ$, the simplifications $\sin(\vartheta) \approx \vartheta$ and $\cos(\vartheta) \approx 1$ are justifiable, so that

$$\vartheta_{\text{flex}} = \frac{-\Omega^2}{k}\left(I_{\eta\eta} - I_{\xi\xi}\right) \cdot \left(\vartheta_{\text{pre}} + \vartheta_{\text{flex}}\right) \Leftrightarrow \vartheta_{\text{flex}} = \frac{\frac{-\Omega^2}{k}\left(I_{\eta\eta} - I_{\xi\xi}\right)\vartheta_{\text{pre}}}{1 + \frac{\Omega^2}{k}\left(I_{\eta\eta} - I_{\xi\xi}\right)} = -0.75^\circ. \tag{23}$$

In VAST, the configuration of Fig. 4 is modeled using the BAM elements described in this paper. Only for this test case, the elongation degrees-of-freedom u are disabled to suppress geometric stiffening, which is not included in the analytical reference calculation. Table 3 compares the resulting flexible-tip twist for $\mathbf{S} = \mathbf{S}_{\text{tra}}$ and $\mathbf{S} = \mathbf{S}_{\text{tra}} - \tilde{\mathbf{u}}_{\text{A}}\,\mathbf{S}_{\text{rot}}$ with the analytical solution. As expected, $\mathbf{S}_{\text{tra}}$ does not account for the effect of the propeller moment at all. However, with $\mathbf{S} = \mathbf{S}_{\text{tra}} - \tilde{\mathbf{u}}_{\text{A}}\,\mathbf{S}_{\text{rot}}$, the result is correct within the accuracy expected from the numerics and discretization.

To address the frequency-domain behavior of the beam, the restoring propeller moment can be interpreted as an additional stiffness k_{p}, for which the small-angle assumption for ϑ is again applied:

$$k_{\text{p}} = \partial M_{\text{p}}/\partial\vartheta = \Omega^2\left(I_{\eta\eta} - I_{\xi\xi}\right). \tag{24}$$

The expected torsional eigenfrequency is $\sqrt{\left(k + k_{\text{p}}\right)/I_{\zeta\zeta}}$ with $I_{\zeta\zeta} = m/12\,\left(c^2 + a^2\right)$. Table 4 presents the first torsion eigenfrequency of the beam for the nonrotating case $\Omega = 0\,\text{rad/s}$ and for $\Omega = 100\,\text{rad/s}$. In the nonrotating case, the numerical results deviate from the analytical reference, which is 9.18790 Hz, by only -0.004%, which confirms the consistency of the analytical and numerical structural models (without inertial loads). At $\Omega = 100\,\text{rad/s}$, a first torsional eigenfrequency of 18.3758 Hz is expected analytically. However, with $\mathbf{S} = \mathbf{S}_{\text{tra}}$, the eigenfrequency remains equal to that of the nonrotating case. With $\mathbf{S} = \mathbf{S}_{\text{tra}} - \tilde{\mathbf{u}}_{\text{A}}\,\mathbf{S}_{\text{rot}}$, the eigenfrequency matches the analytical prediction with an error of only -0.002%.

Table 3 Equilibrium flexible twist ϑ_{flex} of the beam in Fig. 4

Analytical	VAST-BAM, $\mathbf{S} = \mathbf{S}_{\text{tra}}$	VAST-BAM, $\mathbf{S} = \mathbf{S}_{\text{tra}} - \tilde{\mathbf{u}}_{\text{A}}\,\mathbf{S}_{\text{rot}}$
$\vartheta_{\text{flex}} = -0.75000^\circ$	$\vartheta_{\text{flex}} = 0.00000^\circ$	$\vartheta_{\text{flex}} = -0.74996^\circ$

Table 4 First torsion eigenfrequency of the beam in Fig. 4, also with $\Omega = 0\,\text{rad/s}$

Ω	0 rad/s	100 rad/s
Analytical	9.18790 Hz	18.3758 Hz
VAST-BAM, $\mathbf{S} = \mathbf{S}_{\text{tra}}$	9.18756 Hz	9.18756 Hz
VAST-BAM, $\mathbf{S} = \mathbf{S}_{\text{tra}} - \tilde{\mathbf{u}}_{\text{A}}\,\mathbf{S}_{\text{rot}}$	9.18756 Hz	18.3754 Hz

These results show that the complemented shape function matrix is needed to account for the propeller moment. Note that the rotation of the cross-sectional integrals in equations (10)–(12) by $\mathbf{T}$ *must* include the deformation, i.e., $\mathbf{T} = \mathbf{T}(\mathbf{r}_\mathrm{I})$. This is crucial to determine k_p (see equation (24)) because M_p depends on ϑ_flex. The torsion eigenfrequency, in turn, depends on k_p.

3.3 Validation based on a practical test case

As an example of a modern rotor blade, a prototype blade [10] from a helicopter rotor research program at Airbus is investigated. Figure 5 shows the blade with a double-swept planform. The real blade is attached to the rotor hub via a combined bearing that allows flap and lead-lag motion of the blade, and features an elastomeric spring–damper device. Furthermore, a dedicated lead-lag damper is integrated into the blade root. The kinematics of this lead-lag damper along with the blade pitch actuation via control rods constitute multiple load paths, which are not yet supported in VAST. Therefore, a simplified blade-attachment model is used in VAST: The bearing is modeled as a sequence of a flap hinge and a lead-lag hinge. A surrogate rotational flap spring and a surrogate rotational lead-lag spring–damper are applied at the respective hinges. A torsion hinge with a discrete surrogate torsional spring is also introduced – it models the elasticity of the control rod and the swashplate.

Equilibrium calculations are conducted in vacuo at a nominal rotor speed for blade pitch angles within $[-10\,^\circ, 20\,^\circ]$. The elastic tip twist with respect to the FFR is presented in Fig. 6 for both implementations of $\mathbf{S}$ used to calculate $\mathbf{Q}_\mathrm{v}^\mathrm{f}$. At a pitch angle of $10\,^\circ$, a tip twist of $-0.3\,^\circ$ is observed with $\mathbf{S} = \mathbf{S}_\mathrm{tra}$, while $\mathbf{S} = \mathbf{S}_\mathrm{tra} - \tilde{\mathbf{u}}_\mathrm{A}\,\mathbf{S}_\mathrm{rot}$ yields a significantly more pronounced tip twist of $-0.5\,^\circ$. The nonzero tip twist with $\mathbf{S} = \mathbf{S}_\mathrm{tra}$ is explained by the complex blade geometry with a pretwist distribution and a double-swept planform. Accordingly, in contrast to the test case in Fig. 4, the pure consideration of centrifugal loads acting on the blade axis introduces some torsion moments in the beam.

While the results shown in Fig. 6 lack reference data for validation, experimental and numerical reference results are available for the Campbell diagram of the prototype blade, which is presented in Fig. 7. In [10], the blade eigenfrequencies were identified based on a whirl-tower test of the full-scale rotor ("reference, experimental"). Furthermore, the eigenfrequencies were calculated with a standalone FE program ("numerical-BAM") using BAM

Fig. 5 Double-swept prototype blade, picture from [10]

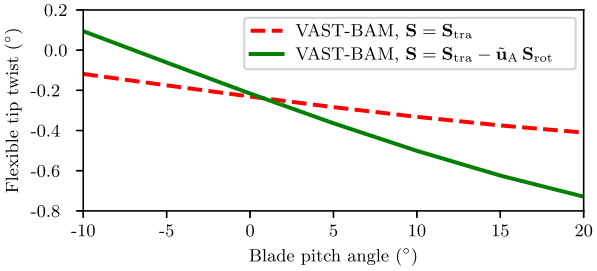

Fig. 6 Equilibrium flexible tip twist with respect to the FFR in vacuo at a nominal rotor speed for different blade pitch angles

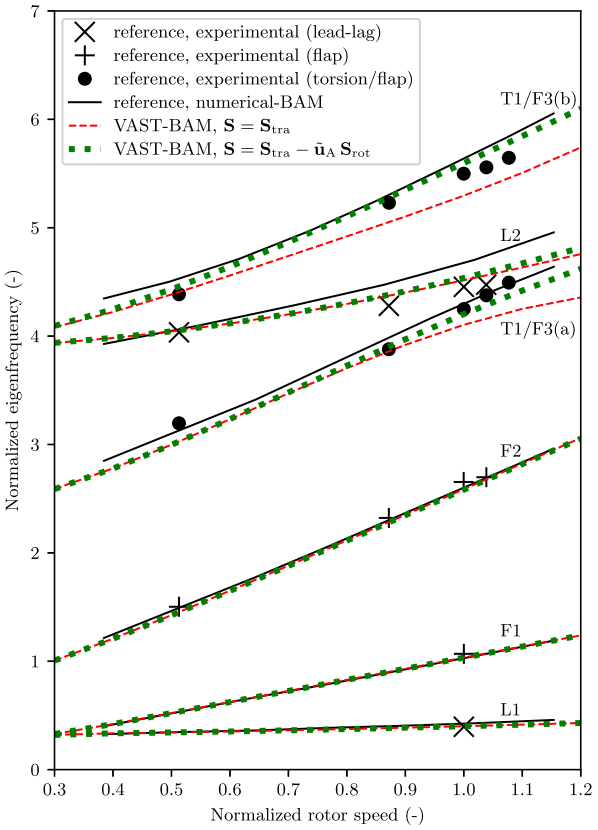

Fig. 7 Campbell diagram of a double-swept rotor blade, modeled with the original and complemented shape function matrices $\mathbf{S}$ for the calculation of $\mathbf{Q}_{\text{v}}^{\text{f}}$, reference results taken from [10]

elements (not MBS-capable). The assignment of mode types (L = lead-lag, F = flap, and T/F = torsion/flap) has been adopted from [10].

The bottom of Fig. 7 shows the first lead-lag mode (×) and the first flap mode (+). These modes feature a negligible deformation of the blade, but primarily contain flap or lead-lag displacements in the respective hinges, so they are rigid-body modes. The correlation is very good between all numerical and experimental results. The two different implementations of $\mathbf{S}$ in VAST-BAM do not cause deviations. The same holds for the second flap mode (+) that includes flexible flap bending of the blade.

In contrast, differences are observed for the torsion/flap modes (●). At a normalized rotor speed of 1.0, the first normalized torsion/flap eigenfrequency T1/F3(a) in the experiment is 4.25. The VAST prediction with $\mathbf{S} = \mathbf{S}_{\text{tra}}$ is 4.11, which is 3% lower than in the experiment. In contrast, the result using $\mathbf{S} = \mathbf{S}_{\text{tra}} - \tilde{\mathbf{u}}_{\text{A}}\,\mathbf{S}_{\text{rot}}$ for calculating $\mathbf{Q}_{\text{v}}^{\text{f}}$ is 4.20, which matches the experimental reference with an error of -1% and also fits the numerical reference better. For the second torsion/flap mode T1/F3(b) with an experimental normalized eigenfrequency of 5.50, the prediction error improves from -5% to $+1\%$. The improvements are even more significant at higher rotor speeds. The second lead-lag mode (×) is marginally affected by the changed implementation of $\mathbf{S}$. This can be explained by a coupling with the T1/F3(a) mode that has an eigenfrequency very close to that of L2. Through this coupling, the propeller moment – that tends to influence torsion modes – may also affect L2. The deviation of both VAST-BAM implementations from the numerical reference, however, is *not* explained

by the effect of the propeller moment. A distinct reason for the overprediction by the numerical reference could not be identified.

As expected, the upgrade from $\mathbf{S} = \mathbf{S}_{\text{tra}}$ to $\mathbf{S} = \mathbf{S}_{\text{tra}} - \tilde{\mathbf{u}}_{\text{A}}\,\mathbf{S}_{\text{rot}}$ in the calculation of $\mathbf{Q}_{\text{v}}^{\text{f}}$ primarily affects the torsion modes of the rotor blade. This can be explained by the effect of the propeller moment, as described in Sect. 3.2. The upgrade is needed to properly predict the torsion eigenfrequencies with the FFR formulation implemented for VAST-BAM.

4 Conclusions

The FFR formulation is used to model helicopter rotor blades as 1D beams within an MBS. To appropriately account for the torsion dynamics of a rotor blade in this approach, rotational shape functions must be considered in the inertia shape integrals and when projecting loads (e.g., centrifugal forces) onto the flexible degrees-of-freedom. This can be achieved by using the complemented shape function matrix, which includes the effect of rotational deflection combined with the beam-axis offset of a particle. The added value of this modified FFR formulation is the consideration of the propeller moment that is demonstrated for an academic test case with analytic reference results. To address a practical test case, a double-swept rotor blade is analyzed. The prediction of the torsion eigenfrequencies significantly improves when using the complemented shape function matrix in the calculation of inertial loads acting on the flexible degrees-of-freedom.

Acknowledgements The authors would like to express their appreciation for the contributions of the entire VAST developer team. Each member played a role in realizing the achievements presented in this work. We are particularly grateful to Maximilian Mindt for his thorough literature research and recommendations regarding the propeller moment. Thank you also to Rémi Coisnon and Yan Skladanek at Airbus Helicopters for their helpful advice toward integrating BAM into VAST.

Supported by:

Federal Ministry
for Economic Affairs
and Climate Action

on the basis of a decision
by the German Bundestag

Author contributions F.W. developed the multibody part of the work (MBS with flexible body interface based on FFR) and wrote the major part of the manuscript. J.M. integrated the Beam Advanced Model into VAST and adapted it to fit the flexible body interface; he wrote the section pertaining to the specifics of BAM. Both authors reviewed the manuscript.

Funding Open Access funding enabled and organized by Projekt DEAL.

Data availability No datasets were generated or analysed during the current study.

Declarations

Competing interests The authors declare no competing interests.

References

1. Bauchau, O.A., Han, S., Mikkola, A., Matikainen, M.K.: Comparison of the absolute nodal coordinate and geometrically exact formulations for beams. Multibody Syst. Dyn. **32**(1), 67–85 (2014). https://doi.org/10.1007/s11044-013-9374-7
2. Bielawa, R.L.: Rotary Wing Structural Dynamics and Aeroelasticity, 2nd edn. American Institute of Aeronautics and Astronautics, Reston (2006)
3. Hofmann, J., Weiss, F., Mindt, M.: A new approach to comprehensive rotorcraft aeromechanics simulation. In: VFS 77th Annual Forum and Technology Display. Online (2021)
4. Houbolt, J.C., Brooks, G.W.: Differential equations of motion for combined flapwise bending, chordwise bending, and torsion of twisted nonuniform rotor blades. NACA TR 1346, Washington, D.C., USA (1958)
5. Johnson, W.: Rotorcraft Aeromechanics. Cambridge University Press, Cambridge (2013)
6. Kontak, M., Röhrig-Zöllner, M., Hofmann, J., Weiß, F.: Automatic differentiation in multibody helicopter simulation. In: Kecskeméthy, A., Flores, F.G. (eds.) Multibody Dynamics 2019, vol. 53, pp. 534–542. Springer, Cham (2020)
7. Schiavo, F., Ferretti, G., Viganò, L.: Object-oriented modelling and simulation of flexible multibody thin beams in Modelica with the finite element method. In: 4th International Modelica Conference, Hamburg, Germany (2005)
8. Shabana, A.A.: Flexible multibody dynamics: review of past and recent developments. Multibody Syst. Dyn. **1**(2), 189–222 (1997). https://doi.org/10.1023/A:1009773505418
9. Shabana, A.A.: Dynamics of Multibody Systems. Cambridge University Press, Cambridge (2005)
10. Skladanek, Y.: Formulation d'un élément fini de poutre pour la dynamique des pales d'hélicoptère de géométrie complexe. Ph.D. thesis, l'Institut National des Sciences Appliquées de Lyon, France (2011)
11. Skladanek, Y., Cranga, P., Ferraris, G., Jacquet, G., Dufour, R.: A nonlinear beam finite element for curved and twisted composite helicopter blade. In: 36th European Rotorcraft Forum, Paris, France (2010)
12. Skladanek, Y., Cranga, P., Ferraris, G., Jacquet, G., Dufour, R.: A highly accurate beam finite element for curved and twisted helicopter blades. In: ASME 2011 International Design Engineering Technical Conferences and Computers and Information in Engineering Conference, Washington, D.C., USA (2011)
13. Skladanek, Y., Boucherie, L., Benoit, B., Cranga, P.: Advanced beam modeling applied to articulated rotor – implementation in HOST aeromechanic simulation tool. In: AHS 70th Annual Forum and Technology Display, Montréal, Québec, Canada (2014)
14. Weiss, F., Merlis, J., Lojewski, R., Hofmann, J., Roehrig-Zoellner, M.: Rotor blade modeling in a helicopter multi body simulation based on the floating frame of reference formulation. In: 48th European Rotorcraft Forum, Winterthur, Switzerland (2022)
15. Wilkie, W.K., Mirick, P.H., Langston, C.W.: Rotating shake test and modal analysis of a model helicopter rotor blade. NASA Technical Memorandum 4760, Langley Research Center, Hampton, Virginia (1997)